Three-dimensional study of Mars upper thermosphere/ionosphere and hot oxygen corona: 1. General description and results at equinox for solar low conditions

Arnaud Valeille,[1] Valeriy Tenishev,[1] Stephen W. Bougher,[1] Michael R. Combi,[1] and Andrew F. Nagy[1]

Received 25 March 2009; revised 2 June 2009; accepted 15 July 2009; published 7 November 2009.

[1] Unlike Earth and Venus, Mars with a weak gravity allows an extended corona of hot species and the escape of its lighter constituents in its exosphere. Being the most important reaction, the dissociative recombination of O_2^+ is responsible for most of the production of hot atomic oxygen deep in the dayside thermosphere/ionosphere. The investigation of the Martian upper atmosphere is therefore complicated by the change in the flow regime from a collisional to a collisionless domain. Past studies, which used simple extrapolations of 1-D thermospheric/ionospheric parameters, could not account for the full effects of realistic conditions, which are shown to be of significant influence on the exosphere both close to and far away from the exobase. In this work, the combination of the new 3-D Direct Simulation Monte Carlo kinetic model and the modern 3-D Mars Thermosphere General Circulation Model is employed to describe self-consistently the Martian upper atmosphere at equinox for solar low conditions. For the first time, a 3-D analysis and shape of the Martian hot corona is provided, along with density and temperature profiles of cold and hot constituents as functions of position on the planet. Atmospheric loss and ion production (found to be more than an order of magnitude lower than the neutral escape), calculated locally all around the planet, provide valuable information for plasma models, refining the understanding of the ion loss, atmospheric sputtering, and interaction with the solar wind, in general.

Citation: Valeille, A., V. Tenishev, S. W. Bougher, M. R. Combi, and A. F. Nagy (2009), Three-dimensional study of Mars upper thermosphere/ionosphere and hot oxygen corona: 1. General description and results at equinox for solar low conditions, *J. Geophys. Res.*, *114*, E11005, doi:10.1029/2009JE003388.

1. Introduction

[2] The understanding of the Martian exosphere is an important subject of interest for the description of the shape of the hot corona, for the evaluation of the atmospheric escape rates and for the resulting estimation of the global loss of water. The neutral components of the exosphere are also the direct source of ion production and thus govern different ionospheric processes, such as interaction with the solar wind and ion loss.

[3] A great improvement in the computational simulations has been made since the pioneering works on the Martian exosphere [*Nagy and Cravens*, 1988; *Ip*, 1990; *Nagy et al.*, 1990; *Lammer and Bauer*, 1991], and a number of theoretical quantitative works have been reported over the past ten years in an attempt to describe the extended hot atomic corona in 1-D spherical symmetry [*Kim et al.*, 1998; *Lammer et al.*, 2000; *Nagy et al.*, 2001; *Krestyanikova and Shematovitch*, 2005; *Cipriani et al.*, 2007]. The major improvement concerns the treatment of the collision processes and the consideration of a transitional domain (between the collision-dominated thermosphere and the collisionless exosphere) in order to take into account the change in the collision regime in the flow. However, those studies are most often specific to the subsolar point (i.e., equatorial noon), cannot account for the important diurnal important variations, and therefore are inherently constrained to a local description of the altitude profile.

[4] In an effort to address this effect, a few studies extended their 1-D spherically symmetric thermosphere input parameters to higher dimensions by simple extrapolation. Distributions varying as a cosine function of Solar Zenith Angle (SZA) were first assumed to extend the inputs to 2-D axisymmetric with respect to the Mars-Sun axis [*Kim et al.*, 2001]. The inclusion of planetary rotation or diurnal tides added some 3-D influences to the results [*Hodges*, 2000; *Chaufray et al.*, 2007]. However, while the improvements in the exosphere model were considerable, the spatial distribution of the results of all these studies still presented the same limitations that were inherent in the 1-D thermosphere inputs upon which they were based [*Hanson et al.*, 1977; *Nier and McElroy*, 1977; *Zhang et al.*, 1990; *Fox*, 1993; *Kim et al.*, 1998; *Krasnopolsky*, 2002]. It has been

[1]Department of Atmospheric, Oceanic and Space Sciences, University of Michigan, Ann Arbor, Michigan, USA.

0148-0227/09/2009JE003388

extensively demonstrated [e.g., *Bell et al.*, 2007; *Bougher et al.*, 2000, 2006, 2008] that the thermosphere exhibits diurnal patterns (such as dynamical effects and abrupt changes in the ionosphere structure), as well as local variations (temperature and wind distributions, planet rotation, polar warming, hemispheric asymmetries) that cannot be treated by simple extrapolation of a 1-D thermosphere. As the entire hot population that defines the corona is produced deep in the thermosphere and interacts with it, it is important that these complex thermospheric patterns are taken into account in any rigorous description of the exosphere.

[5] To address this need, the recent studies couple self-consistently a 2-D exosphere description with 3-D thermosphere/ionosphere inputs by using a combination of the 3-D Mars Thermosphere General Circulation Model (MTGCM) and the 3-D Direct Simulation Monte Carlo (DSMC) kinetic model both for present [*Valeille et al.*, 2009a] and ancient [*Valeille et al.*, 2009b] Mars conditions. Without any further approximations, the MTGCM provides all the parameters needed to evaluate the state of the background thermosphere and the production of hot oxygen atoms at any point around the planet. Exospheric results were presented as a function of SZA.

[6] A full 3-D DSMC which includes the coronal particles and describes the heating of the thermosphere was thought to be computationally too expensive in the past [*Leblanc and Johnson*, 2001]. After design of a 3-D unstructured mesh and improvement of our DSMC model, a complete 3-D detailed description of both the thermosphere/ionosphere and exosphere can be accomplished in a reasonable computational time. The results are presented and discussed in this study.

[7] In addition to allowing a better understanding of the Martian neutral hot corona, a 3-D study of the exosphere provides more insightful inputs for ionospheric studies, such as the local exobase height determination, local ion production, atom-to-molecule ratio variations at the exobase, and information on the nightside where few measurements exist. All these exosphere parameters are critical for current 3-D plasma models (as mentioned in various studies, such as *Brecht* [1997a, 1997b], *Acuña et al.* [1998], *Leblanc and Johnson* [2001, 2002], *Ma et al.* [2002, 2004], *Modolo et al.* [2005], and *Fang et al.* [2008]) that would in turn give more detailed results on ion loss, atmospheric sputtering, and interaction with the solar wind in general. Also certain features, such as magnetic crustal field, which plays an influence on ion loss [e.g., *Fang et al.*, 2009], are localized and therefore can only be modeled in 3-D.

[8] In this paper, both MTGCM and DSMC models constitute our global approach and are presented along with a summary of the main assumptions considered for the generation and collision of hot oxygen atoms in the Martian upper atmosphere. Three-dimensional thermosphere/ionosphere results are presented, discussed and then used as inputs to the DSMC model to provide a detailed 3-D description of the Martian hot corona. Influences of the thermosphere winds, planetary rotation, and local variations of thermosphere/ionosphere input parameters in general are discussed. The description of the exosphere includes escape maps, the 3-D shape of the hot corona, exospheric density profiles, and ion production maps. In the remainder of this paper, and for comparison sake (with Viking measurements and with others models), all calculations are run at the fixed orbital position of equinox and for solar low conditions.

2. Model and Assumptions

[9] In this section, the two models used together in our approach, the MTGCM and the DSMC, are presented along with a summary of the main assumptions used in the description of the Martian upper atmosphere. Both thermospheric/ionospheric and exospheric models, as well as how they are coupled, were previously presented in detail [*Valeille et al.*, 2009a, 2009b]. Upgrades from the 2-D to 3-D description are listed here, including improvements in the hot oxygen production, ionization processes, domain resolution and unstructured mesh.

2.1. Model Description: MTGCM

[10] The MTGCM is a finite difference primitive equation model that self-consistently solves for time-dependent neutral temperatures, neutral ion densities, and three component neutral winds over the globe [*Bougher et al.*, 2004, 2006, 2008, 2009]. MTGCM prognostic and diagnostic thermospheric fields are simulated on 33 pressure levels above 1.32 μbar (corresponding to altitudes of $\sim$70–200 km), with a 5° latitude $\times$ 5° longitude grid resolution. A fast non-Local Thermodynamic Equilibrium (NLTE) 15-μm cooling scheme is implemented, along with corresponding near Infra Red (near IR) heating rates [*López-Valverde et al.*, 1998; *Bougher et al.*, 2006].

[11] The MTGCM is driven from below by the NASA Ames Mars General Circulation Model (MGCM) code [*Haberle et al.*, 1999] at the 1.32 μbar level (near 60–80 km). A detailed upward coupling between the MGCM and MTGCM across this boundary captures migrating, as well as nonmigrating, upward propagating tides. Key prognostic (temperatures, zonal and meridional winds) and diagnostic (geopotential height) fields are passed upward at every MTGCM grid point on 2-min time step intervals. The inclusion of the Ames MGCM provides a realistic lower atmosphere that is critical for achieving an appropriate simulation of the Mars upper atmosphere within the MTGCM domain [*Bougher et al.*, 2006, 2008].

[12] The MGCM-MTGCM framework incorporates a detailed photochemical ionosphere, which captures the major ions, O_2^+, CO_2^+, O^+, and NO^+, below 180 km [*Bougher et al.*, 2004]. This formulation is critical to the self-consistent simulation of dayside atomic oxygen densities in the MGCM-MTGCM upper atmosphere. Atomic oxygen abundances are inferred from UV airglow observations [*Stewart et al.*, 1992; *Huestis et al.*, 2008], and the uncertainty in the measurements impacts the simulation of CO_2 15-μm cooling rates in the Mars dayside and nightside upper atmospheres [*Huestis et al.*, 2008; *Bougher et al.*, 2009].

2.2. Model Description: DSMC

[13] Because the 2-D version of the DSMC approach used in this work was already described in detail in the previous study of *Valeille et al.* [2009a], only a brief summary of the method is given here, followed by the presentation of the challenges and improvements to develop a new 3-D code. The DSMC model is a 3-D simulator that

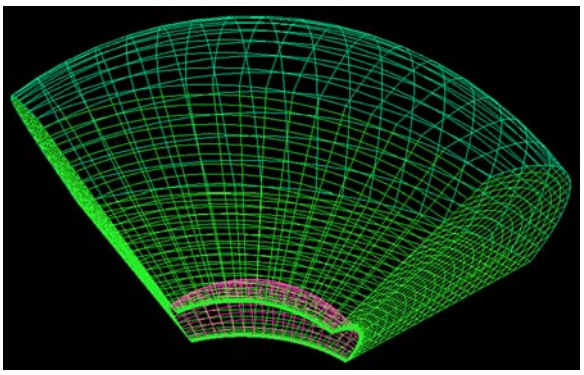

Figure 1. Section of the 3-D tetrahedral mesh. The lower boundary at an altitude of 135 km is represented in pink, the internal cells in light green, and the upper boundary at the altitude of 2 radii (i.e., 3 radii from the center of the planet) in dark green.

solves for the coupled thermosphere/ionosphere and exosphere systems using an altitude-based coordinate system. Instead of assuming a strict separation between collision and collisionless domains, the DSMC model considers a collision transitional domain where the momentum exchange within the flow is still important but the collision frequency is not high enough to maintain equilibrium in the flow. The primary parameters provided by the DSMC code are: specie, weight, position and velocity for each simulated particles. Macroscopic parameters are derived from these, i.e., densities, mean velocities, escape/return fluxes, temperatures, heating, pressure, collision frequencies, various ionization rates, and many others than can be derived directly or indirectly from these.

[14] With the DSMC method, a gas flow is represented by a set of (usually millions) model particles moving in phase space. A probabilistic technique is used to sample the state of collision partners after a momentum exchange event, to simulate scattering and chemical reactions. The approach is based on solving the Boltzmann equation and, hence, is valid for all gas flow regimes presented in the domain of study.

[15] The main constituents of the upper thermosphere are carbon dioxide and atomic oxygen. The trajectory of each hot atom in the gravitational field of Mars is traced from collision to collision until it escapes at 3 radii, becomes part of the "cold" thermosphere when its speed falls below $V_{threshold}$ (which is defined as twice the local thermal speed in the transitional domain), or becomes ionized in the sunlit portion of the exosphere. Scattering collisions are approximated as elastic hard sphere encounters, and O/O and O/CO_2 collision cross sections are taken at 2×10^{-15} cm^2 [*Hodges*, 2000]. Hot atoms can also be created by fairly direct collision of the hot particles with the background thermospheric oxygen atoms if the speed of the collided background atom is above $V_{threshold}$. This secondary source of hot oxygen atoms is found to be far from negligible and accounts for about 20% of the total escape [*Hodges*, 2000; *Valeille et al.*, 2009a].

[16] Aside from capturing 3-D details, several improvements of the previous version of the DSMC code are achieved. The current state of the code includes more photochemical processes and follows more species. Additional impacts of the exosphere onto the thermosphere, such as heating due to the return flux, are now computed. This additional information provided will be presented in a future work. The calculation time is optimized together with the time step adaptation. Scale height extrapolation accounts for change in the local temperature and in the gravity field in the transitional domain. The upper limit of the collision transitional domain is extended to an altitude of 600 km (for clarity and consistency in the comparison with the most extreme cases).

[17] For present Mars conditions, O_2^+ dissociative recombination (DR) is by far the most important source of hot oxygen in the Martian thermosphere. The cumulative effect of the escape processes resulting from the interaction of the solar wind onto the Martian corona (including sputtering and ion escape) appears to be smaller by at least 1 order of magnitude than the contribution due to O_2^+ DR at the present epoch according to recent studies [*Leblanc and Johnson*, 2001; *Chaufray et al.*, 2007]. The excess energies and the measured branching ratios of *Kella et al.* [1997] are used for the main branches of the O_2^+ DR reaction. It is important to note that the O_2^+ DR reaction rate coefficient, used by the thermosphere/ionosphere model (MTGCM) for O_2^+ loss and by the exosphere model (DSMC) for hot O source, should be consistent [*Valeille et al.*, 2009a; J. L. Fox, private communication, 2009]. In this work, this common value is taken from *Mehr and Biondi* [1969]:

$$\alpha = 1.95 \times 10^{-7}(300/\mathrm{Te})^{0.7}\mathrm{cm^3\,s^{-1}} \text{ for Te} < 1200\,\mathrm{K}$$
$$\alpha = 0.75 \times 10^{-7}(1200/\mathrm{Te})^{0.56}\mathrm{cm^3\,s^{-1}} \text{ for Te} > 1200\,\mathrm{K} \quad (1)$$

A different hot oxygen production rate coefficient via O_2^+ DR is considered for electron temperatures above 1200 K (equation (1)). The electron density is used in the thermosphere inputs, leading to a ~10% increase in the production (compared to the dominant ion assumption, $[e^-] = [O_2^+]$), in agreement with Viking measurements that suggested that O_2^+ constitutes about 90% of the total ion density [*Hanson et al.*, 1977].

[18] The model provides maps of the three main ionization processes, i.e., photoionization (PI), charge exchange (CE), and electron impact (EI), as explained in detail in the study of [*Valeille et al.*, 2009b]. The respective PI, CE, and EI frequencies are derived from previous studies [*Stebbings et al.*, 1964; *Cravens et al.*, 1987; *Bailey and Sellek*, 1990]. Estimated positions of the ionopause and bow shock [*Zhang et al.*, 1993; *Leblanc and Johnson*, 2001; *Trotignon et al.*, 2006] are used. In the region between the ionopause and the bow shock, the solar wind velocity and density are estimated to be 0.25 and 4 times their respective values above the bow shock in each case.

2.3. Unstructured Mesh

[19] The code uses an unstructured mesh of tetrahedral cells that allows a pertinent description of the domain around complex 3-D bodies (a section of it is shown on Figure 1). It can be easily adapted to the physical features of the problem, and takes into account the variations of the outputs of interest.

[20] The mesh is first generated in hexagonal cells. The three spatial dimensions of a typical cell of the mesh shall

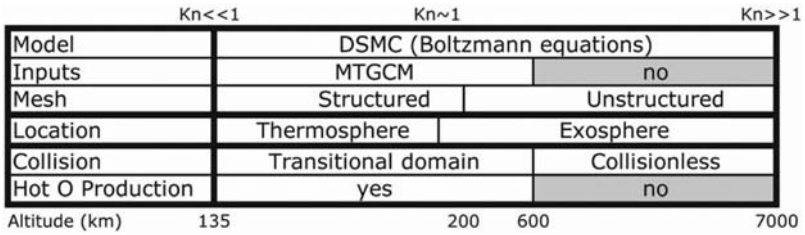

Figure 2. Illustration of the necessity of combining hydrodynamic and kinetic models to describe rigorously both transitional and collisionless regions, adapted from *Valeille et al.* [2009a]. The Knudsen number, $Kn = \lambda/H$, is a dimensionless number defined as the ratio of the molecular mean free path length λ to the scale height H, a representative physical length scale. Collisionless kinetic theory models, used to describe the exosphere, are valid in the limit $Kn \rightarrow \infty$; whereas hydrodynamic models, such as the MTGCM, are used to describe the thermosphere and are valid when the mean free path λ is very small and $Kn \rightarrow 0$. However, the Boltzmann equation of kinetic theory is valid for the whole range of Knudsen numbers and is solved by the DSMC code.

match the three local characteristic lengths of the 3-D problem. The angular resolution matches that of the thermosphere model, being a $5^\circ \times 5^\circ$ grid (i.e., about 300 km $\times$ 300 km at the equatorial surface) all across the simulation domain. However, to capture the critical variations in density with altitude satisfactorily, the radial resolution should be less than about one half to one third of the local scale height in the transitional domain. The mesh presents uniformly spaced cells distributed radially from the inner boundary (at 135 km) to 200 km with a 4 km altitude resolution, followed by exponentially distributed cells beyond the 200 km altitude, as shown in Figure 2. This allows for an approximately constant number of atmospheric particles per cell (mostly $\sim$20–40 particles per cell). Each of those stretched hexagonal cells is then split into six tetrahedral cells.

[21] It should be noted that to keep the same $5^\circ \times 5^\circ$ angular resolution from 2-D to 3-D, a factor 72 in the number of the cells is needed when building a mesh. A factor 3 should be also considered to go from 2-D triangular to 3-D tetrahedral cells. To keep a reasonable computing time and expense, a limitation in the size of the mesh and a decrease in the radial distribution compared to the 2-D mesh [*Valeille et al.*, 2009a, 2009b] are adopted. The 2-D results are however reproduced by corresponding 3-D simulations within less than a 5% error. The two main processes for the generation of the exospheric population, i.e., production (via O_2^+ DR) and collision (with O and CO_2 background species), are well simulated. The size of the simulation domain is limited to a 3 Mars radius, the domain of interest of most studies, in order to limit the computational time and to keep the two-body approximation valid. A total of about 500 000 cells, or 30 million particles, is simulated.

2.4. Three-Dimensional Validation

[22] As this work may be the first 3-D coupled description of the Martian thermosphere/ionosphere and exosphere, a comparison can only be made with a similar study of lower dimension. The model presented here was previously run along 2-D axisymmetric "cuts" through the Martian upper atmosphere in the framework of the study of *Valeille et al.* [2009a]. Those results were reasonably consistent with most of the works of the last ten years [*Kim et al.*, 1998; *Lammer et al.*, 2000; *Hodges*, 2000; *Kim et al.*, 2001; *Krestyanikova and Shematovitch*, 2005; *Cipriani et al.*, 2007; *Chaufray et al.*, 2007]. The coupling of 3-D thermospheric/ionospheric inputs with a 2-D exospheric description suggested in particular that varying equatorial longitude and polar latitude cuts (study path from 0° to 180° SZA along the equator or through the Poles) presented the greatest contrast of thermospheric/ionospheric features and are essentially the two extreme spatial dimensions of the Martian upper atmosphere environment [*Valeille et al.*, 2009a]. These significant differences (yielding about a 30% change in the local escape flux), explained by the seasonal features in the lower atmosphere and the polar warming effect [*Bougher et al.*, 2006], illustrate that the use of a 3-D model would be more appropriate to account for spatial variations of thermospheric/ionospheric parameters. The profiles of the macroscopic exospheric parameters are not homogeneous with respect to the location and a two-dimensional axisymmetric model may be insufficient to describe in detail the entire Martian exosphere.

[23] For testing purposes, the 2-D exospheric results of the study of *Valeille et al.* [2009a] with respect to SZA were first reproduced using the full 3-D code for the same fixed conditions of equinox solar low. Calculations were then performed with full 3-D thermospheric/ionospheric inputs with the current 3-D DSMC model and compared with the previous 2-D axisymmetric calculations along both equatorial and polar cuts. The integration of the hot oxygen escape flux of our 3-D simulation appears between the two extreme spatial cuts as defined and expected by the 2-D study of *Valeille et al.* [2009a], providing a good validation of the computational approach and computer code of the current 3-D model.

2.5. Framework

[24] In this work, the 3-D Cartesian frame for the exosphere description is associated with the Sun. It has its origin at the center of the planet, the x axis pointing toward the Sun, the y axis toward the east terminator and the z axis toward the north pole. Latitudes are counted positively in the northern hemisphere (0° to $+90^\circ$, from equator to north pole) and negatively in the southern hemisphere (0° to -90°, from equator to north pole). Longitudes are counted from the meridian taken here, for simplicity sake, as the half of the great circle going through the subsolar point (i.e., the

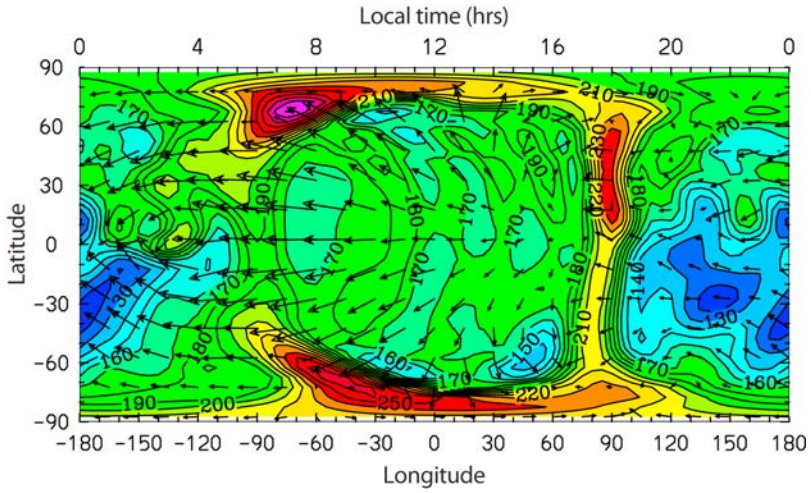

Figure 3. Neutral temperature at an altitude of 190 km. Horizontal wind velocities are represented in the frame associated with Mars by arrows (maximum of ~490 m s^{-1}). Minimum temperatures are in blue and correspond to 115–130 K, while maximum temperatures are in red and correspond to 250–290 K (10 K increments).

noon meridian). They are counted positively toward east (0° to +180°, from noon to midnight through dusk) and negatively toward west (0° to −180°, from noon to midnight through dawn).

[25] The frame associated with Mars can also be considered for the thermosphere description and rotates around the *z* axis with a sidereal rotation period of ~24.6 h toward east (like Earth), i.e., at an equatorial surface speed of ~240 m s^{-1}. It is important to note that, since steady state conditions are assumed in this framework (i.e., it is assumed that the results would not be affected very much by the longitudinal variations during the course of a planet day), the 0° longitude is fixed at local noon (UT = 12).

3. Results and Discussion: Thermosphere/Ionosphere

[26] In this section, the description of the thermosphere by the 3-D MTGCM is presented. It includes maps of the main macroscopic physical parameters, such as CO_2, O and O_2^+ density profiles, neutral, ion and electron temperatures, and winds, as functions of position on the planet, in the frame associated with Mars. For comparison sake (with Viking measurements and with other models), all calculations are run at the fixed orbital position of equinox and for solar low conditions (i.e., solar longitude, Ls, of 180° and F10.7cm of 70 at Earth).

3.1. Temperatures and Winds

[27] The map of simulated MTGCM neutral temperatures in the isothermal region of the Martian upper atmosphere is presented in Figure 3. The average temperature, T∞, of about 170–180 K is mostly located at low and middle latitudes on the dayside and high latitudes on the nightside (green areas in Figure 3). High temperatures are found on the dayside along the terminator (yellow areas in Figure 3), with maxima of about 250–290 K being at the polar regions and in the vicinity of the evening terminator (red areas in Figure 3). Minima of about 115–130 K are situated in the southern hemisphere, at low and middle latitudes on the nightside (blue areas in Figure 3).

[28] Day and nighttime Martian thermospheres were shown to follow similar profile trends in the 120–280 km region, revealing neutral temperature increases with altitude first, and then becoming isothermal above some level [*Valeille et al.*, 2009b]. This level is reached at lower altitudes at night (140–150 km) compared to day (160–170 km). However, it is important to note that the upper atmosphere presents an isothermal structure up to a certain altitude where the temperature profile presents a sharp transition between the cold and hot populations. This transition occurs at altitudes of about 400–600 km for the conditions considered and is further discussed in section 4.3.

[29] A 3-D simulation permits the incorporation of effects of dynamics, which play an important role, especially for the transport of light species. Dynamics can also be seen as a thermostat, changing the heat budget from the dayside to the nightside. Indeed, while thermal conduction heats the nightside, it is also a major cooling mechanism together with Infra Red (IR) 15-μ cooling on the dayside, balancing the solar heating due to EUV and Near Infra Red (NIR).

[30] In the frame associated with Mars, although the Coriolis effect can be seen at the high latitudes as a deviation to the right in the north hemisphere and to the left in the south (see Figure 3), thermospheric winds flow essentially westward at low to middle latitudes. While the wind speed reaches its minimum along the evening terminator, a maximum of about 490 m s^{-1} is located along the morning terminator. At the equator, in the vicinity of the exobase, the planetary rotation speed of 240 m s^{-1} is comparable to the average thermospheric wind speed, but is oriented in the opposite direction. Therefore, in the frame associated with the Sun, the cumulative effect of winds and planetary rotation can be roughly seen as a diurnal tide, as thermospheric flow diverges essentially from near the warm subsolar point and converges near the antisolar point (i.e., equatorial midnight) on the nightside. While such a simple

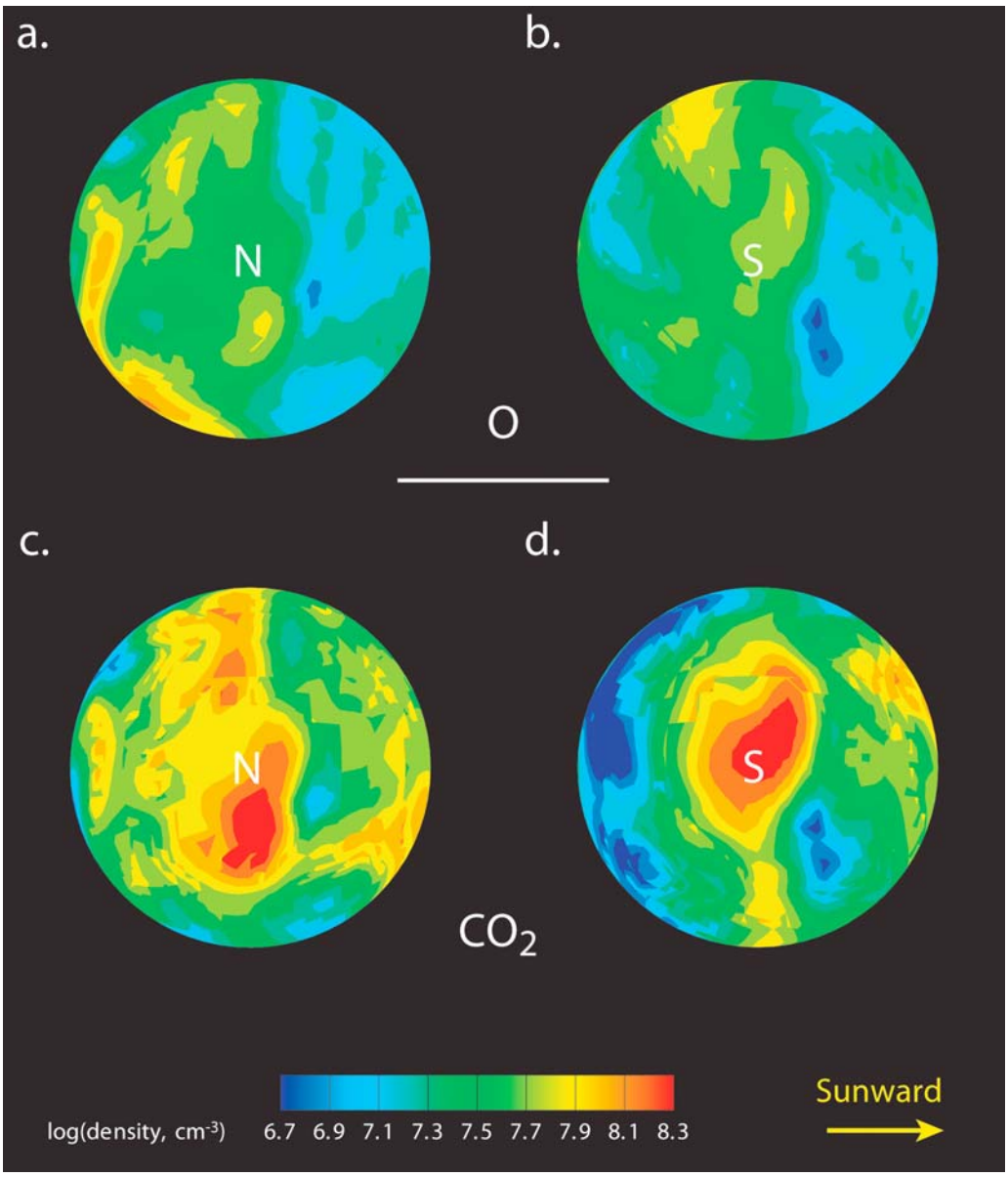

Figure 4. O density maps at the (a) northern and (b) southern hemispheres; CO_2 density maps at the (c) northern and (d) southern hemispheres at an altitude of 190 km. The same color scale is used for Figures 3a–3d. The north and south pole positions are indicated by their initials N and S, respectively. The yellow arrow points toward the Sun.

assumption is correct to first order, the inputs used in this research account for more complex local features, as shown in Figure 3.

[31] Jeans escape is very temperature-dependent and, because the thermal contrast in the exosphere can be very important (more than 120 K between extrema, according to Figure 3), its spatial variations are dramatic. However, even at its local maximum, the thermal escape remains orders of magnitude smaller than nonthermal processes for atomic oxygen. For lighter species, such as hydrogen, Jeans escape can vary as much as a factor of about 150 for constant bulk density from one location to another. Therefore, accounting for these important variations, the 1-D Chamberlain approach used by all hydrogen studies to date [e.g., *Anderson and Hord*, 1971; *Anderson*, 1974; *Nagy et al.*, 1990; *Lichtenegger et al.*, 2004; *Chaufray et al.*, 2008], and which assumes constant exospheric temperatures and spatially uniform densities, can only provide a ±1–2 order of magnitude estimate of escape at best. A 3-D coupling of both thermosphere and exosphere, as well as a better understanding of the spatial density distribution of atomic hydrogen would be helpful in order to obtain a better characterization of the hydrogen escape.

3.2. O and CO_2 Density Distribution

[32] The two main constituents in the Martian upper thermosphere are CO_2 and O. Interestingly, although they exhibit a similar average abundance at an altitude of 190 km, their local distribution is very different. The CO_2 molecule is heavier; therefore its concentration is more responsive to

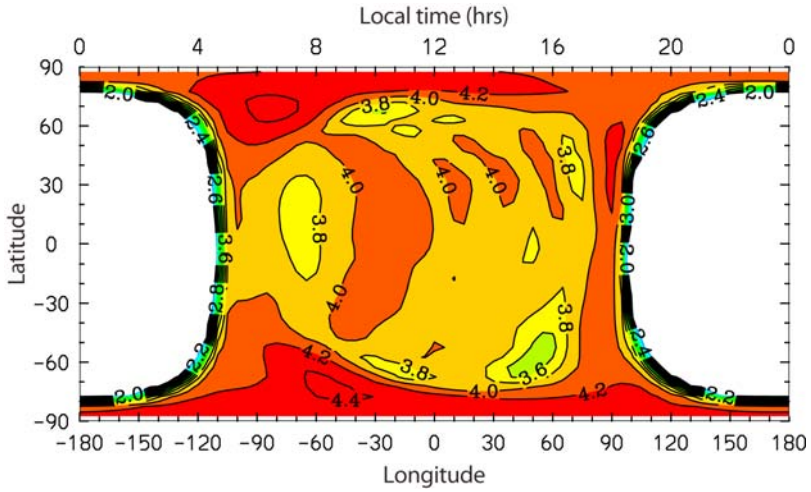

Figure 5. Surface map of O_2^+ ion log density (in cm^{-3}) at an altitude of 190 km. Maximum densities are shown in red and correspond to $\sim 1.6-2.5 \times 10^4$ cm^{-3}.

the local background temperature. Atomic O is lighter, and thus more responsive to transport (i.e., to local temperature gradients). These responses should be put in context using the map of temperature and winds (Figure 3) in order to understand the variations in density presented in Figure 4 (all parameters are shown at the same altitude of 190 km in Figures 2 and 3).

[33] Atomic oxygen reaches its maximum densities at low latitudes on the nightside near the morning terminator (yellow-orange areas in Figure 4), whereas minima are achieved on the dayside close to the evening terminator (light blue areas in Figure 4). These extrema occur at the same positions as the strong convergent nightside and weak divergent dayside winds, consistent with the fact that O density variations are driven by the effect of dynamics. As a result, O density variations are also lower (factor $\sim$10 between extrema) and smoother than the heavier CO_2 (factor $\sim$40 between extrema), as transport, more effective on light species, tends to homogenize the densities. Carbon dioxide reaches its maximum densities in the polar regions where temperatures are warmer (orange-red areas in Figure 4). Similarly, minima are reached at low latitudes on the nightside near the morning terminator where temperatures are colder (dark blue areas in Figure 4). The variations in the local temperature (factor $\sim$2 between extrema, according to Figure 3) affect the scale heights of the constituents in proportion. They vary from 15 to 35 km and from 6 to 14 km for O and CO_2, respectively. The mean altitude of the Martian dayside homopause at equinox for solar low condition is evaluated to be at about 120 km [*Stewart*, 1987; *Bougher et al.*, 2000]. The day and night atmosphere density profiles of both constituents were presented and discussed in the work of *Valeille et al.* [2009b] in good agreement with the only in situ measurements available, by the Viking Lander 1 [*Hanson et al.*, 1977; *Nier and McElroy*, 1977].

3.3. O_2^+ Density Distribution and Ion Peak

[34] O_2^+ is the main ion of the Martian ionosphere. It is a critical parameter for the determination of the hot corona. Its production occurs on the dayside and is directly related to the local background densities of CO_2 and O, the main parent in the photodissociation and charge exchange reactions:

$$\begin{cases} CO_2 + h\nu \rightarrow CO_2^+ + e \\ CO_2^+ + O \rightarrow O_2^+ + CO \end{cases} \quad (2)$$

O_2^+ reaches its maximum density at the same position as CO_2, i.e., in the polar regions, as shown at an altitude of 190 km in Figure 5 and in Figures 4c and 4d for O_2^+ and CO_2, respectively. On the dayside, the difference in O_2^+ density can be as high as of a factor of about 6 and the scale height varies from 8 to 19 km.

[35] The ionospheric peak is found deep in the thermosphere at an altitude of $\sim$122 km at the subsolar point. On the dayside, its height is expected to rise with increasing SZA, as a result of the integration over a longer atmospheric slant path. Its magnitude is expected to decrease with increasing SZA, due to the geometry of the problem and to the extinction of ionizing solar radiation. Along the equator, the ion peak height increases from $\sim$122 to $\sim$126, and then to $\sim$134 km at 0°, 60° and 75° longitude, respectively. The magnitude of the electron concentration is $\sim 1.8 \times 10^5$ cm^{-3} at the subsolar point (can be compared to the O_2^+ concentration presented in the work of *Valeille et al.* [2009b]) and decreases by a factor $\sim$0.6 and $\sim$0.4 from 0° to 60° and 0° to 75° longitude, respectively. These results are in general agreement with both theory and reported observations from Viking [*Zhang et al.*, 1990], Mars Global Surveyor (MGS) [*Withers and Mendillo*, 2005] and Mars Express (MEX) [*Morgan et al.*, 2008].

[36] Interestingly, the results presented in this study suggest that, because of higher concentrations of ions in the polar region compared to lower latitudes, the magnitude of the ion peak undergoes a milder decrease with SZA along a meridian than along the equator. For the same reason, a sharper increase of the ion peak height is expected along a meridian. This latter result agrees with the concerns developed from the MARSIS observations on MEX [*Morgan et al.*, 2008] and suggests that the Martian ionosphere presents

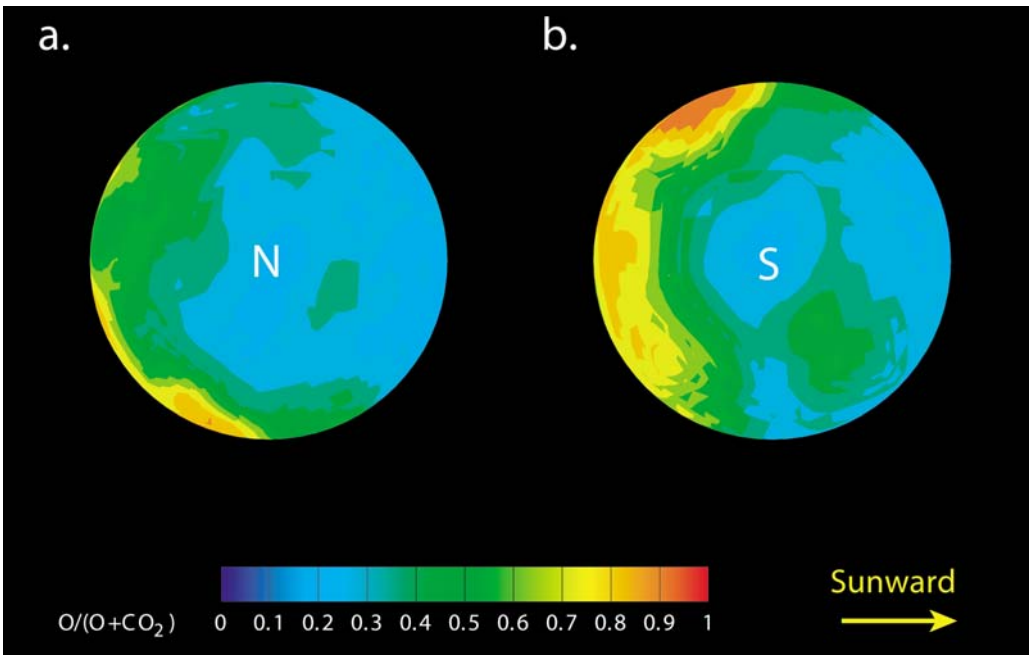

Figure 6. Maps of the oxygen mixing ratio, $X_O = O/(O + CO_2)$, at the (a) northern and (b) southern hemispheres at an altitude of 190 km, above which O becomes the main neutral constituent of the Martian upper thermosphere on the average. The same color scale is used for Figures 5a and 5b. The north and south pole positions are indicated by their initials N and S, respectively. The yellow arrow points toward the Sun.

asymmetries that need to be treated locally (rather than being a homogeneous Chapman layer).

3.4. Atom-to-Molecule Ratio

[37] The O to CO_2 ratio, sometimes called atom-to-molecule ratio (noted $r_{a/m}$), is a particularly important parameter of the Martian upper atmosphere, as it affects locally the exobase height, the ion production, the plasma heating, as well as the escape loss due to incident pickup ions [*Leblanc and Johnson*, 2002].

[38] The work of *Valeille et al.* [2009b] already noticed that the level above which O becomes the main neutral thermospheric constituent undergoes important variations with SZA along the equator. This study shows that this level may vary from an altitude as low as 150 km to an altitude as high as 230 km locally around the planet. The averaged level is at an altitude of about 190 km. Figure 6 shows the O mixing ratio, X_O, a direct function of $r_{a/m}$, at that altitude:

$$X_O = r_{a/m}/(1 + r_{a/m}). \tag{3}$$

[39] It shows that at that altitude, often assumed as the "traditional" exobase height by previous studies [e.g., *Schunk and Nagy*, 2000], neither O nor CO_2 can be rigorously considered as the dominant specie. Indeed from Figure 6, X_O varies from less than 0.1 at the polar regions and at low latitudes north (blue areas in Figure 6) to more than 0.9 at low latitudes south (orange areas in Figure 6). Those important spatial variations in the X_O ratio are explained by the disparities in O and CO_2 abundances, varying both significantly and for different reasons (see section 3.2). As discussed in section 3.3, the ion production is expected to be higher at places where CO_2 is dominant locally. The plasma heating would also be higher, whereas the sputtering yield and the escape loss due to incident pickup ions should decrease due to a lower atom-to-molecule ratio [*Leblanc and Johnson*, 2002].

3.5. Exobase Determination

[40] A traditional definition of the exobase for a 1-D problem is, for a single constituent atmosphere [e.g., *Schunk and Nagy*, 2000],

$$\int_{r_c}^{\infty} \sigma n(r) dr = \sigma n(r_c) H(r_c) = \frac{H(r_c)}{\lambda(r_c)} = 1. \tag{4}$$

This is the level where the collision mean free path equals the temperature scale height of the constituent. However, and as illustrated above, Mars upper atmosphere presents two major neutral constituents, and their mixing ratio varies greatly both with altitude and with position on the planet. Therefore, definition 5 should be modified for a more rigorous determination.

[41] The definition of the local (i.e., for a given angular position) exobase level proposed in this paper is: the level above which an escaping particle moving along a radial direction will encounter one collision on average. This is a more general definition; it is in agreement with the previous definition for a 1-D single constituent problem (equation (4)), and can also be used for a 3-D multiconstituent problem. It should be noted that this is a conservative estimate of the exobase height, as in 3-D, particles below that level are close to an isotropic distribution and therefore are more likely to collide than a purely radially moving particle. The

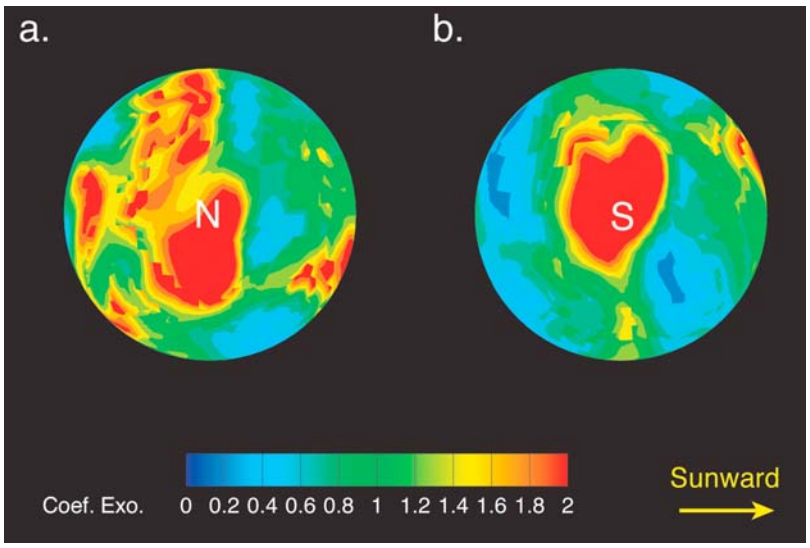

Figure 7. Maps of the exobase criterion at the (a) northern and (b) southern hemispheres at an altitude of 170 km. The same color scale is used for Figures 6a and 6b. The north and south pole positions are indicated by their initials N and S, respectively. The yellow arrow points toward the Sun.

criterion, e(**r**), a function of the position, **r**, is defined as follows and equals to 1 at the local position of the exobase, r_c (i.e., when $r = r_c$):

$$e(r_c) = \sigma_{CO_2} n_{CO_2}(r_c) H_{CO_2}(r_c) + \sigma_O n_O(r_c) H_O(r_c) = 1. \quad (5)$$

It is defined locally and depends on the density of the bulk atmosphere, the mixing ratio of O/CO_2 and the temperature. So, on Figure 7, the local exobase corresponds to the given altitude of 170 km in green areas, is below it in blue areas, and above it in red areas.

[42] The exobase height follows roughly the temperature variations and reaches its lowest value of 155 km along the dayside terminator and at nightside low to middle latitudes, whereas its highest value of 195 km can be found in the polar regions. An average altitude of about 170 km can be found graphically (where most of the surface is found within a small range of the criterion). A 2-D axisymmetric study of the exobase height along the equator, as done in the work of *Valeille et al.* [2009b], may then slightly underestimate the altitude of this level.

4. Results and Discussion: Exosphere

[43] The 3-D MTGCM calculations provide the respective thermospheric/ionospheric inputs for the 3-D DSMC model, which in turn gives a detailed description of the Martian hot corona. In this section, the atmospheric loss due to O_2^+ DR is calculated, as is the ion production above the ionopause, which provides a generous upper limit for ion escape. As already mentioned and for comparison sake (with Viking measurements and with others models), all calculations are run at the fixed orbital position of equinox and for solar low conditions. These specific conditions have been systematically used in the past by modelers and serve as an example to illustrate the general structure and attributes of a 3-D exosphere produced by a self-consistent 3-D thermosphere/ionosphere model.

4.1. Impacts of Local Thermospheric/Ionospheric Asymmetries

[44] The principal advantages that a 3-D study present compared to 2-D include the influences of the thermosphere winds, the planetary rotation and the local features of thermosphere/ionosphere input parameters in general. Most suprathermal oxygen atoms, which define the Martian hot corona, are produced deep in the thermosphere and interact with it by collision. Therefore, the exospheric population is greatly affected by the distribution of the thermosphere/ionosphere parameters. In the previous section of this paper, the thermosphere/ionosphere is shown to exhibit diurnal patterns (such as dynamical effects and abrupt changes in the ionosphere structure), as well as local nonaxisymmetric variations (temperature and wind distributions, planet rotation, polar warming, hemispheric asymmetries). It is natural to expect the exosphere to exhibit similar features.

[45] Asymmetries in thermal and density structure of both the thermosphere (Figures 4, 6, and 7) and ionosphere (Figure 5) are responsible for local variations in the production (see equation (1)) and collision processes (see equation (4)), affecting more significantly the exospheric distribution closer to the exobase.

[46] As mentioned in section 3.1, the planetary rotation equatorial speed is comparable to the average thermospheric wind speed in the Martian upper thermosphere. The impact of both parameters on a particle position depends on the time the particle spends in the system. The more time the particle spends in the system, the farther it is shifted away from its original "windless" direction. Consequently, these impacts on the ballistic trajectories are more noticeable farther from the exobase and affect the general shape of the entire hot corona. An additional horizontal component of 240 m s^{-1} in the initial speed could result in a significant shift (corresponding to 20° SZA) in the position of an nonescaping particle at a distance of 3 Martian radii from the center of the planet. Therefore, thermospheric winds and planetary rotation exhibit comparable and sizable impacts

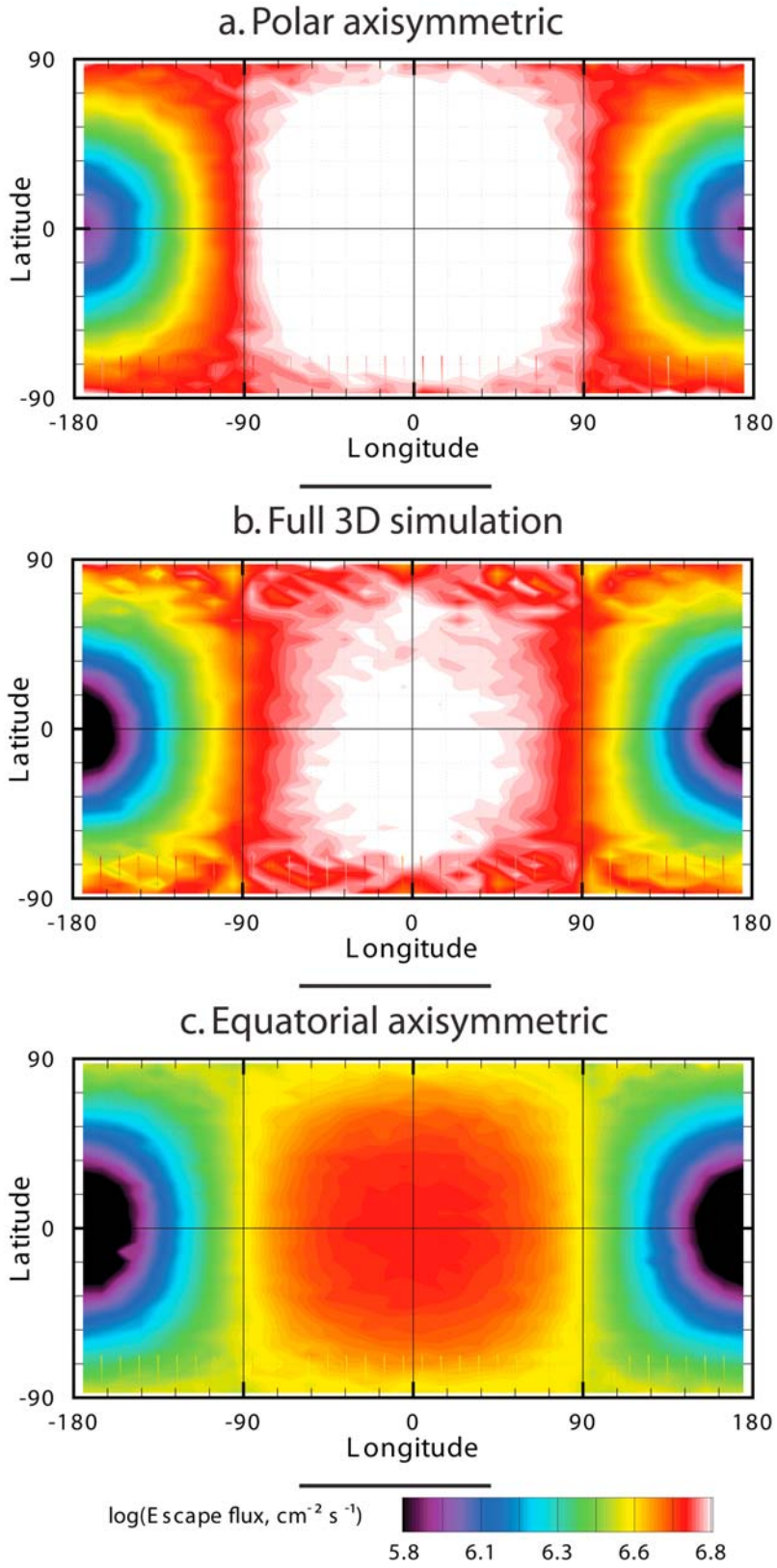

Figure 8. Flux of escaping hot oxygen atoms as functions of longitude and latitude at an altitude surface of 2 Martian radii (∼7000 km) in the frame associated with the Sun. (a) Results from 2-D axisymmetric inputs along the polar meridian. (b) Results from 3-D inputs. (c) Results from 2-D axisymmetric inputs along the equator. Thermospheric winds and planetary rotation are included in Figure 7b only.

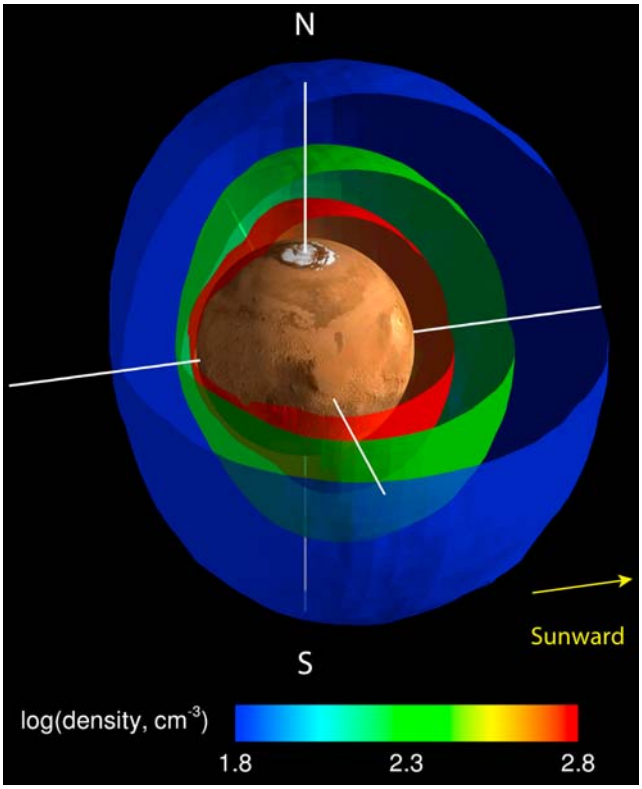

Figure 9. Three-dimensional representation of the Martian hot corona. Three isodensity surfaces of hot atomic oxygen are shown, decreasing with increasing distance from the planet: red, 600 cm^{-3}; green, 200 cm^{-3}; blue, 60 cm^{-3}. The north and south pole positions are indicated by their initials N and S, respectively. The yellow arrow points toward the Sun.

on the density profiles and consequently, on the ionization rates and even more on the return flux of particles to the thermosphere.

[47] As far as we know, only one study [*Hodges*, 2000] considered the effects that thermospheric winds could have on the exospheric distribution of velocities by assuming simple diurnal tides (although Figure 3 above would suggest a different assumption). Hodges concluded that the velocity distribution would be affected by a slight shift with respect to the escape speed. The study of *Chaufray et al.* [2007], which considers exclusively planetary rotation, reports an understandable difference between morning and evening terminator density profile. However, since thermospheric winds and planetary rotation present important similar effects, they need to be addressed together. They are both nonaxisymmetric parameters and therefore cannot inherently be produced by 2-D simulations.

4.2. Escape Flux

[48] Figure 8 shows the results of three different sets of thermosphere/ionosphere inputs onto the escape fluxes of hot oxygen atoms at 3 Martian radii (i.e., at an altitude of ~7000 km).

[49] The 2-D axisymmetric inputs along the polar meridian (Figure 8a) and along the equator (Figure 8c) were characterized as the two most extreme spatial features of the Martian thermosphere/ionosphere in the 2-D study of *Valeille et al.* [2009a]. As expected, these 3-D simulations of extrapolated 2-D axisymmetric thermosphere inputs, similarly adopted by previous studies [*Hodges*, 2000; *Chaufray et al.*, 2007] give rather simple solutions. Escape fluxes are on average 30% higher for the simulation along the pole, due mostly to the higher production of hot oxygen by O_2^+ DR in the polar region.

[50] As expected from the study of *Valeille et al.* [2009a], the results of the full 3-D calculation stand between these two spatial extremes. The spatial integration of the flux leads to an estimated escape rate of 6.0×10^{25} s^{-1}. Rather than an axisymmetric circular shape, the escape flux of hot oxygen, as shown in Figure 4b, exhibits an oblong shape extended toward the poles. Also, the atmospheric loss is slightly larger in the south than it is in the north due to the hemispheric asymmetries, topographic differences and the dust distribution characterized in the lower atmosphere inputs.

[51] Although there is no production on the nightside of the planet, a low escape flux (of about an order of magnitude smaller than on the dayside) is calculated at 3 radii in the vicinity of the antisolar point. In contrast, the study of *Valeille et al.* [2009a] reported a difference of only a factor 3–4 between the subsolar and the antisolar points at an altitude of 10 radii. This abrupt decrease in the diurnal variations of the escape flux with an increasing distance from the center of the planet is explained by the cumulative effect of collisions in the transitional domain, presence of nightside ions in the vicinity of the terminator, and more importantly trajectory curvature due to gravity.

4.3. Hot Corona

[52] The resolution of the 3-D unstructured mesh reveals the full density distribution of both cold and hot components (the criteria is defined in section 2.2) of the atomic oxygen population. The latter allows a description of the shape of the Martian hot corona, as shown in Figure 9 with three isodensity levels.

[53] In the vicinity of the exobase (170 km altitude) and below, the oxygen population is cold. Density profiles extracted along 1-D columns at different positions around the planet exhibit a scale height temperature that matches the average neutral temperature of $T\infty \sim 170$ K. Density maxima of $\sim 2 \times 10^8$ cm^{-3} are found at low latitudes on the nightside, whereas minima of $\sim 2 \times 10^7$ cm^{-3} are reached along the dayside terminator in the vicinity of the exobase. Therefore, a factor of about 10 is observed in the spatial variation around the planet at this altitude.

[54] In contrast, at higher altitudes (above ~600 km altitude), the oxygen population is hot and the scale height temperature is about T_{hot} ~4000 K. Maxima of ~60 cm^{-3} are located south of the subsolar point and minima of ~12 cm^{-3} are achieved at the vicinity of the antisolar point at an altitude of 7000 km. As a result, the shape of the hot corona is clearly inflated toward the dayside (Figure 9). However, the important diurnal density variation decreases with altitude (from a factor ~30 near the exobase to a factor ~5 at an altitude of 7000 km), due to a very efficient transfer along ballistic trajectories, in agreement with the results of previous studies [*Kim et al.*, 2001; *Valeille et al.*, 2009a]. Further above (7000 km to 10 radii), temperatures

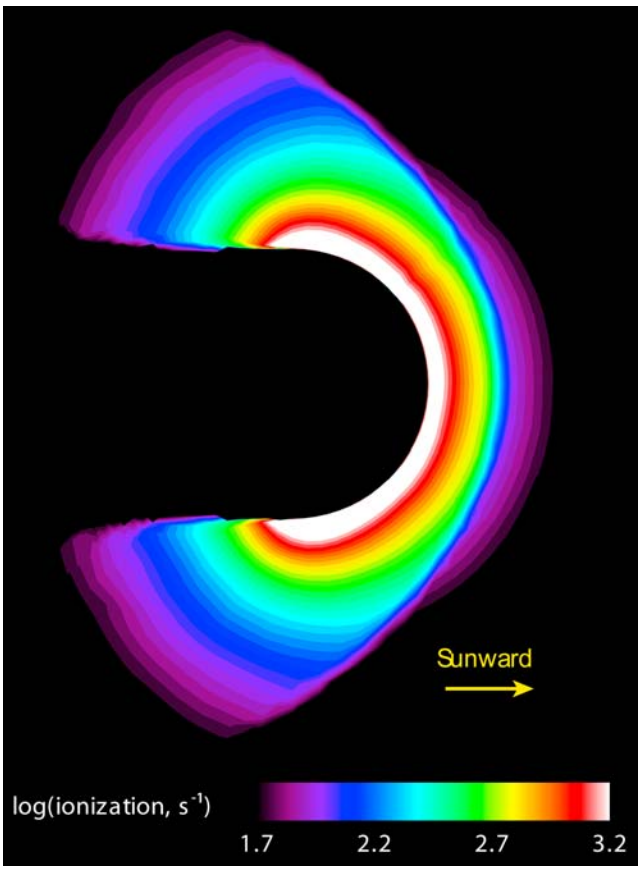

Figure 10. O^+ ionization rate (in s^{-1}) in the equatorial section. The yellow arrow points toward the Sun.

decrease due to expansion and a study over an extended domain [*Valeille et al.*, 2009a] reports a scale height temperature of about ~1500 K and a diurnal density variation of a factor ~3.

[55] The hot oxygen component should begin to dominate above the cold background atmosphere at an average altitude of about 500 km [*Lammer et al.*, 2000; *Lichtenegger et al.*, 2007; *Valeille et al.*, 2009a] above the Martian surface for the conditions considered. As both exospheric and thermospheric oxygen profiles change spatially in a 3-D description, this transition level varies between ~400 km (vicinity of the subsolar point) to ~600 km altitude. In this region, the cold-to-hot O ratio increases from 0.01 to 100 in less than 50 km. Consequently, the neutral temperatures are expected to exhibit a sharp transition between a cold and hot isothermal structure (from $T\infty \sim 170$ K to $T_{hot} \sim 4000$ K).

[56] While a dramatic diurnal variation is seen in the escape fluxes close to the planet due to the absence of production on the nightside (section 4.2), it is not the case in the density distribution, which is rather smooth by comparison. The main difference is that nonescaping energetic particles keep interacting with the thermosphere after they leave the exobase by bouncing. This mechanism is presented and discussed in the study of *Valeille et al.* [2009a] and contributes to populate the nightside efficiently.

4.4. O^+ Ion Production

[57] Figure 10 shows the simulated total ionization rate in the Martian extended ionosphere after summation of the three main ionization contributions. In this study, both relative contributions of cold and hot oxygen particles can be considered, and they are shown comparable for each ionization process. Integration gives a total O^+ ion production of 2.2×10^{24} s^{-1}, in good agreement with the recent study of *Chaufray et al.* [2007] (1.9×10^{24} s^{-1} for solar low condition). This latter study, together with the work of *Valeille et al.* [2009b] that reported a value of 1.5×10^{24} s^{-1}, used axisymmetric equatorial inputs and therefore is likely to underestimate the total production, due to asymmetries in the atomic oxygen distribution. Under the generous assumption that all ions produced above the ionopause escape, the computed O^+ ion loss would then be in excellent agreement with the value of $\sim 2.4 \times 10^{24}$ s^{-1} based on data obtained with new energy settings for the ASPERA-3 ion mass analyzer (IMA) on MEX reported in the recent study of *Lundin et al.* [2008]. However, if only 10 to 35% of ions produced are considered to escape, as suggested by some studies [*Chaufray et al.*, 2007; *Fang et al.*, 2008], then the estimation of the O^+ ion loss should be scaled down by an order of magnitude. This value would be closer to the one of $\sim 1.6 \times 10^{23}$ s^{-1} derived from the measurements of the same instrument using original energy settings [*Barabash et al.*, 2007]. Even in its most generous estimation (of 2.2×10^{24} s^{-1}), the ion loss remains more than an order of magnitude less than the hot oxygen escape of 6.0×10^{25} s^{-1}.

5. Conclusion

[58] In this study, the combination of the new 3-D DSMC kinetic model and the 3-D MTGCM is used to provide the first self-consistent 3-D description of the Martian upper atmosphere. All calculations are made at a fixed orbital position of equinox and for solar low conditions.

[59] Previous studies of the Martian hot corona could not incorporate the full effects of realistic upper atmospheric conditions and the spatial distribution of their results based upon the same limitations inherent to the 1-D thermosphere/ionosphere inputs. In agreement with the reported modern observations, the 3-D calculations of the MTGCM show that important local asymmetries should be taken into account (in addition to the diurnal patterns) for a rigorous description of the upper atmosphere. Local variations in winds, temperatures and background species relative abundances lead to a new perspective on the exobase height determination, atom-to-molecule ratio and on the ionosphere structure (ion peak height, local ion production), that in turn affect production and collision of hot oxygen atoms, critical exospheric mechanisms at the origin of the hot corona and atmospheric loss.

[60] Asymmetries in thermal and density structure affect more significantly the exospheric distribution closer to the exobase, whereas the comparable and sizable nonaxisymmetric effects of thermospheric winds and planetary rotation are more noticeable farther from it. Isodensity maps illustrate the 3-D shape of the Martian hot corona, which is clearly inflated toward the dayside. Rather than an axisymmetric circular shape, the escape flux of hot oxygen exhibits an oblong shape extended toward the poles. The computed O escape rate due to O_2^+ DR is 6.0×10^{25} s^{-1} and the total O^+ ionization rate above the ionopause is estimated at $2.2 \times$

10^{24} s^{-1}. Therefore, even in its most generous estimation, the ion loss remains more than an order of magnitude less than the hot oxygen escape due to O_2^+ DR.

[61] While hot oxygen density and escape flux vary significantly with position on the planet and altitude (diurnal difference of a factor of about 3–4 at 10 radii), the studies of *Valeille et al.* [2009a, 2009b] suggest that variations of the same order can be expected over the solar cycle with changing orbital position and season, and over Martian history. Therefore, in order to obtain a complete description of this physical problem and an estimation of the global loss of water at Mars, these most limiting cases need to be addressed in detail in a future study.

[62] Coupled results of the thermosphere/ionosphere with the exosphere, similar to those presented and discussed in this paper, would be useful for complex 3-D plasma models, since exospheric parameters govern different local ionospheric processes, such as ion loss, atmospheric sputtering and interaction with the solar wind in general. It would also permit a better understanding of localized features, such as magnetic crustal fields which can only be modeled in 3-D. The combined results of the 3-D MTGCM and DSMC are currently being used in the framework of an intercomparison of global models and measurements of the Martian plasma environment, a working group of the International Space Sciences Institute (ISSI) [*Brain et al.*, 2008].

[63] **Acknowledgments.** Support for this work comes from the NASA Mars Fundamental Research grant NNG05GL80G and the Mars Data Analysis Program grant NNX07AO84G. Computations were performed on the massively parallel Columbia computer at the High-End Computing (HEC) Program's NASA Advanced Supercomputing (NAS) Facility. The author would like to thank Marco Ceze of the Aerospace Engineering department of the University of Michigan for his help in the design of the 3-D unstructured mesh. The authors thank the referees for their assistance in evaluating this paper.

References

Acuña, M. H., et al. (1998), Magnetic field and plasma observations at Mars: Initial results of the Mars Global Surveyor mission, *Science*, *279*, 1676–1680, doi:10.1126/science.279.5357.1676.

Anderson, D. E. (1974), Mariner 6, 7 and 9 Ultraviolet Spectrometer Experiment: Analysis of hydrogen Lyman alpha data, *J. Geophys. Res.*, *79*, 1513–1518, doi:10.1029/JA079i010p01513.

Anderson, D. E., and C. W. Hord (1971), Mariner 6 and 7 Ultraviolet Spectrometer Experiment: Analysis of hydrogen Lyman alpha data, *J. Geophys. Res.*, *76*, 6666–6673, doi:10.1029/JA076i028p06666.

Bailey, G. J., and R. Sellek (1990), A mathematical model of the Earth's plasmasphere and its application in a study of He+ at L = 3, *Ann. Geophys.*, *8*, 171–190.

Barabash, S., A. Fedorov, R. Lundin, and J.-A. Sauvaud (2007), Martian atmospheric erosion rates, *Science*, *315*, 501–503, doi:10.1126/science.1134358.

Bell, J. M., S. W. Bougher, and J. R. Murphy (2007), Vertical dust mixing and the interannual variations in the Mars thermosphere, *J. Geophys. Res.*, *112*, E12002, doi:10.1029/2006JE002856.

Bougher, S. W., S. Engel, R. G. Roble, and B. Foster (2000), Comparative terrestrial planet thermospheres: 3. Solar cycle variation of global structure and winds at solstices, *J. Geophys. Res.*, *105*, 17,669–17,692, doi:10.1029/1999JE001232.

Bougher, S. W., S. Engel, D. P. Hinson, and J. R. Murphy (2004), MGS Radio Science electron density profiles: Interannual variability and implications for the neutral atmosphere, *J. Geophys. Res.*, *109*, E03010, doi:10.1029/2003JE002154.

Bougher, S. W., J. M. Bell, J. R. Murphy, P. G. Withers, and M. López-Valverde (2006), Polar warming in the Mars lower thermosphere: Seasonal variations owing to changing insolation and dust distributions, *Geophys. Res. Lett.*, *33*, L02203, doi:10.1029/2005GL024059.

Bougher, S. W., P.-L. Blelly, M. Combi, J. L. Fox, I. Mueller-Wodarg, A. Ridley, and R. G. Roble (2008), Neutral upper atmosphere and ionosphere modeling, *Space Sci. Rev.*, *139*, 107–141, doi:10.1007/s11214-008-9401-9.

Bougher, S. W., T. M. McDunn, K. A. Zoldak, and J. M. Forbes (2009), Solar cycle variability of Mars dayside exospheric temperatures: Model evaluation of underlying thermal balances, *Geophys. Res. Lett.*, *36*, L05201, doi:10.1029/2008GL036376.

Brain, D., et al. (2008), Intercomparison of global models and measurements of the Martian plasma environment, technical report, Int. Space Sci. Inst. Bern.

Brecht, S. H. (1997a), Hybrid simulations of the magnetic topology of Mars, *J. Geophys. Res.*, *102*, 4743–4750, doi:10.1029/96JA03205.

Brecht, S. H. (1997b), Solar wind proton deposition into the Martian atmosphere, *J. Geophys. Res.*, *102*, 11,287–11,294, doi:10.1029/97JA00561.

Chaufray, J. Y., R. Modolo, F. Leblanc, G. Chanteur, R. E. Johnson, and J. G. Luhmann (2007), Mars solar wind interaction: Formation of the Martian corona and atmospheric loss to space, *J. Geophys. Res.*, *112*, E09009, doi:10.1029/2007JE002915.

Chaufray, J. Y., J. L. Bertaux, F. Leblanc, and E. Quémerais (2008), Observation of the hydrogen corona with SPICAM on Mars Express, *Icarus*, *195*, 598–613, doi:10.1016/j.icarus.2008.01.009.

Cipriani, F., F. Leblanc, and J. J. Berthelier (2007), Martian corona: Nonthermal sources of hot heavy species, *J. Geophys. Res.*, *112*, E07001, doi:10.1029/2006JE002818.

Cravens, T. E., J. U. Kozyra, A. F. Nagy, T. I. Gombosi, and M. Kurtz (1987), Electron impact ionization in the vicinity of comets, *J. Geophys. Res.*, *92*, 7341–7353, doi:10.1029/JA092iA07p07341.

Fang, X., M. W. Liemohn, A. F. Nagy, Y. Ma, D. De Zeeuw, J. U. Kozyra, and T. H. Zurbuchen (2008), Pickup oxygen ion velocity space and spatial distribution around Mars, *J. Geophys. Res.*, *113*, A02210, doi:10.1029/2007JA012736.

Fang, X., M. W. Liemohn, A. F. Nagy, J. G. Luhmann, and Y. Ma (2009), On the effect of the Martian crustal magnetic field on atmospheric erosion, *Icarus*, doi:10.1016/j.icarus.2009.01.012, in press.

Fox, J. L. (1993), On the escape of oxygen and hydrogen from Mars, *Geophys. Res. Lett.*, *20*, 1747–1750.

Haberle, R. M., M. M. Joshi, J. R. Murphy, J. R. Barnes, J. T. Schofield, G. Wilson, M. López-Valverde, J. L. Hollingsworth, A. F. C. Bridger, and J. Schaeffer (1999), General circulation model simulations of the Mars Pathfinder atmospheric structure investigation/meteorology data, *J. Geophys. Res.*, *104*, 8957–8974, doi:10.1029/1998JE900040.

Hanson, W. B., S. Santanini, and D. R. Zuccaro (1977), The Martian ionosphere as observed by Viking retarding potential analyszers, *J. Geophys. Res.*, *82*, 4351–4363, doi:10.1029/JS082i028p04351.

Hodges, R. R. (2000), Distributions of hot oxygen for Venus and Mars, *J. Geophys. Res.*, *105*, 6971–6981, doi:10.1029/1999JE001138.

Huestis, D. L., S. W. Bougher, J. L. Fox, M. Galand, R. E. Johnson, J. I. Moses, and J. C. Pickering (2008), Cross sections and reaction rates for comparative planetary aeronomy, *Space Sci. Rev.*, *139*, 63–105, doi:10.1007/s11214-008-9383-7.

Ip, W. H. (1990), The fast atomic oxygen corona extent of Mars, *Geophys. Res. Lett.*, *17*, 2289–2292, doi:10.1029/GL017i013p02289.

Kella, D., P. J. Johnson, H. B. Pederson, L. Vejby-Christensen, and L. H. Andersen (1997), The source of green light emission determined from a heavy-ion storage ring experiment, *Science*, *276*, 1530–1533, doi:10.1126/science.276.5318.1530.

Kim, J., A. F. Nagy, J. L. Fox, and T. E. Cravens (1998), Solar cycle variability of hot oxygen atoms at Mars, *J. Geophys. Res.*, *103*, 29,339–29,342, doi:10.1029/98JA02727.

Kim, Y. H., S. Son, Y. Yi, and J. Kim (2001), A non-spherical model for the hot oxygen corona of Mars, *J. Korean Astron. Soc.*, *34*, 25–29.

Krasnopolsky, V. A. (2002), Mars' upper atmosphere and ionosphere at low, medium, and high solar activities: Implications for evolution of water, *J. Geophys. Res.*, *107*(E12), 5128, doi:10.1029/2001JE001809.

Krestyanikova, M. A., and V. I. Shematovitch (2005), Stochastic models of hot planetary and satellite coronas: A photochemical source of hot oxygen in the upper atmosphere of Mars, *Sol. Syst. Res.*, *39*, 22–32.

Lammer, H., and S. J. Bauer (1991), Nonthermal atmospheric escape from Mars and Titan, *J. Geophys. Res.*, *96*, 1819–1825, doi:10.1029/90JA01676.

Lammer, H., W. Stumptner, and S. J. Bauer (2000), Upper limits for the Martian exospheric number density during the planet B/Nozomi mission, *Planet. Space Sci.*, *48*, 1473–1478, doi:10.1016/S0032-0633(00)00095-7.

Leblanc, F., and R. E. Johnson (2001), Sputtering of the Martian atmosphere by solar wind pick-up ions, *Planet. Space Sci.*, *49*, 645–656, doi:10.1016/S0032-0633(01)00003-4.

Leblanc, F., and R. E. Johnson (2002), Role of molecular species in pickup ion sputtering of the Martian atmosphere, *J. Geophys. Res.*, *107*(E2), 5010, doi:10.1029/2000JE001473.

Lichtenegger, H. I. M., H. Lammer, D. F. Vogl, and S. J. Bauer (2004), Temperature effects of energetic neutral hydrogen on the Martian exosphere, *Adv. Space Res.*, *33*, 140–144, doi:10.1016/j.asr.2003.07.018.

Lichtenegger, H. I. M., H. Lammer, Y. N. Kulikov, S. Kazeminejad, G. H. Molina-Cuberos, R. Rodrigo, B. Kazeminejad, and G. Kirchengast (2007), Effects of low energetic neutral atoms on Martian and Venusian dayside exospheric temperature estimations, *Space Sci. Rev.*, *126*, 469–501, doi:10.1007/s11214-006-9082-1.

López-Valverde, M. A., D. P. Edwards, M. López-Puertas, and C. Roldán (1998), Nonlocal thermodynamic equilibrium in general circulation models of the Martian atmosphere: 1. Effects of the local thermodynamic equilibrium approximation on thermal cooling and solar heating, *J. Geophys. Res.*, *103*, 16,799–16,812, doi:10.1029/98JE01601.

Lundin, R., S. Barabash, M. Holmström, H. Nilsson, M. Yamauchi, M. Fraenz, and E. M. Dubinin (2008), A comet-like escape of ionospheric plasma from Mars, *Geophys. Res. Lett.*, *35*, L18203, doi:10.1029/2008GL034811.

Ma, Y., A. F. Nagy, K. C. Hansen, D. L. De Zeeuw, and T. I. Gombosi (2002), Three-dimensional multispecies MHD studies of the solar wind interaction with Mars in the presence of crustal fields, *J. Geophys. Res.*, *107*(A10), 1282, doi:10.1029/2002JA009293.

Ma, Y., A. F. Nagy, I. V. Sokolov, and K. C. Hansen (2004), Three-dimensional, multispecies, high spatial resolution MHD studies of the solar wind interaction with Mars, *J. Geophys. Res.*, *109*, A07211, doi:10.1029/2003JA010367.

Mehr, F. J., and M. A. Biondi (1969), Electron temperature dependence of recombination of O_2^+ and N_2^+ ions with electrons, *Phys. Rev.*, *181*, 264–271, doi:10.1103/PhysRev.181.264.

Modolo, R., G. M. Chanteur, E. Dubinin, and A. P. Matthews (2005), Influence of the solar activity on the Martian plasma environment, *Ann. Geophys.*, *23*, 433–444.

Morgan, D. D., D. A. Gurnett, D. L. Kirchner, J. L. Fox, E. Nielsen, and J. J. Plaut (2008), Variation of the Martian ionospheric electron density from Mars Express radar soundings, *J. Geophys. Res.*, *113*, A09303, doi:10.1029/2008JA013313.

Nagy, A. F., and T. E. Cravens (1988), Hot oxygen atoms in the upper atmosphere of Venus and Mars, *Geophys. Res. Lett.*, *15*, 433–435, doi:10.1029/GL015i005p00433.

Nagy, A. F., J. Kim, and T. E. Cravens (1990), Hot hydrogen and oxygen atoms in the upper atmosphere of Venus and Mars, *Ann. Geophys.*, *8*, 251–256.

Nagy, A. F., M. W. Liemohn, J. L. Fox, and J. Kim (2001), Hot carbon densities in the exosphere of Mars, *Geophys. Res. Lett.*, *82*, 4341–4349.

Nier, A. O., and M. B. McElroy (1977), Composition and structure of Mars' upper atmosphere: Results from the neutral mass spectrometers on Viking 1 and 2, *J. Geophys. Res.*, *82*, 4341–4349, doi:10.1029/JS082i028p04341.

Schunk, R. W., and A. F. Nagy (2000), *Ionospheres*, Cambridge Univ. Press, New York.

Stebbings, R. F., A. C. H. Smith, and H. Erhardt (1964), Charge transfer between oxygen atoms and O+ and H+ ions, *J. Geophys. Res.*, *69*, 2349–2355, doi:10.1029/JZ069i011p02349.

Stewart, A. I. F. (1987), Revised time dependent model of the Martian atmosphere for use in orbit lifetime and sustenance studies, *LASP-JPL Internal Rep., PO# NQ-802429*, Jet Propul. Lab., Pasadena, Calif.

Stewart, A. I. F., M. J. Alexander, R. R. Meier, L. J. Paxton, S. W. Bougher, and C. G. Fesen (1992), Atomic oxygen in the Martian thermosphere, *J. Geophys. Res.*, *97*, 91–102, doi:10.1029/91JA02489.

Trotignon, J. G., C. Mazelle, C. Bertucci, and M. H. Acuna (2006), Martian shock and magnetic pile-up boundary positions and shapes determined from Phobos 2 and Mars Global Surveyor data sets, *Planet. Space Sci.*, *54*, 357–369, doi:10.1016/j.pss.2006.01.003.

Valeille, A., M. R. Combi, V. Tenishev, S. W. Bougher, and A. F. Nagy (2009a), A study of suprathermal oxygen atoms in Mars upper thermosphere and exosphere over the range of limiting conditions, *Icarus*, doi:10.1016/j.icarus.2008.08.018, in press.

Valeille, A., S. W. Bougher, V. Tenishev, M. R. Combi, and A. F. Nagy (2009b), Water loss and evolution of the upper atmosphere and exosphere over Martian history, *Icarus*, doi:10.1016/j.icarus.2009.04.036, in press.

Withers, P., and M. Mendillo (2005), Response of peak electron densities in the Martian ionosphere to day-to-day changes in solar flux due to solar rotation, *Planet. Space Sci.*, *53*, 1401–1418, doi:10.1016/j.pss.2005.07.010.

Zhang, M. H. G., J. G. Luhmann, and A. J. Kliore (1990), An observational study of the nightside ionospheres of Mars and Venus with radio occultation methods, *J. Geophys. Res.*, *95*, 17,095–17,102, doi:10.1029/JA095iA10p17095.

Zhang, M. H. G., J. G. Luhmann, and A. F. Nagy (1993), Oxygen ionization rates at Mars and Venus: Relative contributions of impact ionization and charge exchange, *J. Geophys. Res.*, *98*, 3311–3318, doi:10.1029/92JE02229.

S. W. Bougher, M. R. Combi, A. F. Nagy, V. Tenishev, and A. Valeille, Department of Atmospheric, Oceanic and Space Sciences, Space Research Building, University of Michigan, 2455 Hayward Street, Ann Arbor, MI 48109-2143, USA.